Accepted Manuscript

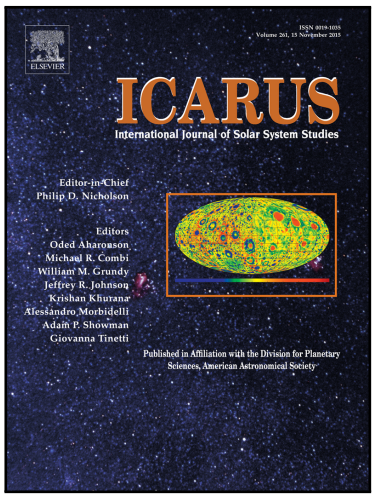

Comparison of areas in shadow from imaging and altimetry in the north polar region of Mercury and implications for polar ice deposits

Ariel N. Deutsch , Nancy L. Chabot , Erwan Mazarico , Carolyn M. Ernst , James W. Head , Gregory A. Neumann , Sean C. Solomon

PII: S0019-1035(16)30299-8
DOI: 10.1016/j.icarus.2016.06.015
Reference: YICAR 12102

To appear in: *Icarus*

Received date: 14 December 2015
Revised date: 6 May 2016
Accepted date: 18 June 2016

Please cite this article as: Ariel N. Deutsch , Nancy L. Chabot , Erwan Mazarico , Carolyn M. Ernst , James W. Head , Gregory A. Neumann , Sean C. Solomon , Comparison of areas in shadow from imaging and altimetry in the north polar region of Mercury and implications for polar ice deposits, *Icarus* (2016), doi: 10.1016/j.icarus.2016.06.015

Comparison of areas in shadow from imaging and altimetry in the north polar region of Mercury and implications for polar ice deposits

Ariel N. Deutsch[a,*], Nancy L. Chabot[b], Erwan Mazarico[c], Carolyn M. Ernst [b], James W. Head[a], Gregory A. Neumann[c], and Sean C. Solomon[d,e]

[a]*Department of Earth, Environmental and Planetary Sciences, Brown University, Providence, RI 02912, USA*

[b]*The Johns Hopkins University Applied Physics Laboratory, Laurel, MD 20723, USA*

[c]*NASA Goddard Space Flight Center, Greenbelt, MD 20771, USA*

[d]*Lamont-Doherty Earth Observatory, Columbia University, Palisades, NY 10964, USA*

[e]*Department of Terrestrial Magnetism, Carnegie Institution of Washington, Washington, D.C. 20015, USA*

[*]Corresponding author. Tel.: +17034705234.

Highlights ***(3-5 bullet points, maximum 85 characters, spaces included, per bullet)*****:**

- Shadows near Mercury's north pole were mapped from MESSENGER images and altimetry.
- Radar-bright deposits collocate with areas of persistent and permanent shadow.
- This collocation is consistent with a dominantly water-ice composition.
- Many regions of persistent or permanent shadow lack radar-bright deposits.
- Shadowed regions lacking radar-bright deposits do not correlate with insolation.

ABSTRACT

Earth-based radar observations and results from the MESSENGER mission have provided strong evidence that permanently shadowed regions near Mercury's poles host deposits of water ice. MESSENGER's complete orbital image and topographic datasets enable Mercury's surface to be observed and modeled under an extensive range of illumination conditions. The shadowed regions of Mercury's north polar region from 65°N to 90°N were mapped by analyzing Mercury Dual Imaging System (MDIS) images and by modeling illumination with Mercury Laser Altimeter (MLA) topographic data. The two independent methods produced strong agreement in identifying shadowed areas. All large radar-bright deposits, those hosted within impact craters ≥6 km in diameter, collocate with regions of shadow identified by both methods. However, only ~46% of the persistently shadowed areas determined from images and ~43% of the permanently shadowed areas derived from altimetry host radar-bright materials. Some sizable regions of shadow that do not host radar-bright deposits experience thermal conditions similar to those that do. The shadowed craters that lack radar-bright materials show a relation with longitude that is not related to the thermal environment, suggesting that the Earth-based radar observations of these locations may have been limited by viewing geometry, but it is also possible that water ice in these locations is insulated by anomalously thick lag deposits or that these shadowed regions do not host water ice.

Keywords

Mercury; Ices; Radar observations; Image processing

1. Introduction

More than two decades ago, Earth-based radar images of Mercury first revealed an area of high radar backscatter near the planet's north pole (Slade et al., 1992; Butler et al., 1993). Observations made at the Arecibo Observatory confirmed the presence of radar-bright materials at Mercury's north pole and indicated similar materials near the planet's south pole (Harmon and Slade, 1992). Because the radar characteristics of Mercury's polar deposits are similar to those of water ice at the Martian polar caps and the icy outer solar system satellites, and because the locations of the deposits coincided with impact craters in Mariner 10 images of polar regions where available (Harmon et al., 1994, 2001, 2011; Harmon 2007), these materials have been interpreted as water-ice deposits on the shadowed portions of crater floors. Early thermal models constructed for idealized flat-floored crater shapes indicated that the permanently shadowed regions near Mercury's poles provide thermal environments capable of hosting stable water-ice deposits on geologic timescales (Paige et al., 1992).

More recently, the MErcury Surface, Space ENvironment, GEochemistry, and Ranging (MESSENGER) spacecraft returned a broad range of evidence confirming that these radar-bright materials are predominantly water ice. The spacecraft's Neutron Spectrometer (NS) documented enhanced concentrations of hydrogen in Mercury's north polar region, quantitatively consistent with models in which all radar-bright polar deposits consist primarily of water ice (Lawrence et al., 2013). Maps of shadowed regions derived from images captured by the Mercury Dual Imaging System (MDIS) (Hawkins et al., 2007) showed that all major radar-bright deposits collocate with regions of permanent shadow in the south polar region (Chabot et al., 2012) and with areas of persistent shadow – i.e., shadowed in all images acquired – in the north polar

region (Chabot et al., 2013). Mercury Laser Altimeter (MLA) (Cavanaugh et al., 2007) measurements of reflectance at 1064 nm wavelength (Neumann et al., 2013) and MDIS imaging (Chabot et al., 2014) of the radar-bright deposits in the shadowed north polar craters revealed low-reflectance surfaces that extend to the edges of shadowed areas and terminate with sharp boundaries. On the basis of thermal models, these low-reflectance surfaces are interpreted to consist of a surficial layer of volatile organic-rich materials, formed as lag deposits, which insulate water ice beneath them (Paige et al., 2013). Thermal models also indicate that the floors of some higher-latitude craters near the north pole can support long-lived water ice exposed at the surface without the need for an insulating layer (Paige et al., 2013). MLA reflectance (Neumann et al., 2013) and MDIS imaging observations (Chabot et al., 2014) revealed a high-reflectance surface on a radar-bright polar deposit on the floor of one such crater, Prokofiev, suggesting that water ice is exposed at the surface in this crater.

Earlier mapping of shadowed areas in Mercury's north polar region (Chabot et al., 2013) was from images acquired during the first Earth year of MESSENGER's orbital mission. After its first year of operations, MESSENGER had not yet achieved full coverage of Mercury, and, in particular, there were substantial gaps in the north polar region because of MESSENGER's non-polar orbit inclination (Solomon et al., 2007). This incomplete image coverage limited mapping of persistently shadowed regions from MDIS images and left a gap from ~86°N to 90°N (Chabot et al., 2013). Previously unmapped regions include craters with large radar-bright deposits (>10 km in horizontal extent), an unresolved radar-bright "diffuse patch," and craters predicted by thermal models as able to host surface water ice deposits (Paige et al., 2013). Additionally, the previous measurements of persistent shadow were made from a limited MDIS dataset of ~6500 images with which the majority of the polar surface had been imaged approximately 10–20 times

(Chabot et al., 2013). This dataset allowed for the identification of only those persistently shadowed craters ≥10 km in diameter. Similarly, incomplete MLA coverage of this region after MESSENGER's first year of operations required interpolated measurements to model the topography north of 84°N, limiting the resolution and accuracy of thermal models in the northernmost area (Paige et al., 2013).

The full image dataset now available provides more than 16,000 images useful for mapping shadows in Mercury's north polar region from 65°N poleward, and every point on Mercury's surface in this latitude range was imaged. Furthermore, with these images we are able to identify small craters (<10 km in diameter) with simple bowl-shaped morphologies as persistently shadowed. Moreover, MESSENGER acquired just over four years of MLA data from orbit before impacting Mercury's surface on 30 April 2015. This complete orbital dataset offers the opportunity to map topography and shadows in Mercury's north polar region to a level of detail that was not previously possible.

Here we map regions of persistent shadow in Mercury's north polar region with two independent methods. With MDIS images, we map persistent shadow following the methods of Chabot et al. (2013), but with a more robust dataset that covers the entire north polar region and under an extensive range of illumination conditions. Regions of persistent shadow are again defined as those that remain in shadow in all orbital images. We also model regions of permanent shadow in Mercury's north polar region from MLA topographic data, with a method similar to that used to identify permanently shadowed regions on the Moon (Mazarico et al., 2011). Regions of permanent shadow are defined as those that are modeled to be in shadow by illumination models derived from topography. With shadows in Mercury's north polar region from 65°N to 90°N determined from full orbital datasets by both methodologies, we compare the

strengths and limitations of each shadow map. We also compare the spatial distribution of regions of shadow with that of deposits identified from Earth-based radar observations, and we discuss the implications for water ice on Mercury.

2. Methods

2.1. Mapping Shadows from MDIS Imagery

During just over four years of orbital operations, MDIS imaged Mercury's north polar region with repeated imaging campaigns. In particular, the MDIS wide-angle camera (WAC) provided images of Mercury's surface under a range of illumination conditions that revealed the planet in different degrees of shadow. MDIS was also equipped with a narrow-angle camera (NAC), but the NAC footprint, with a 1.5° field of view, was considerably smaller than that from the 10.5° field of view of the WAC and provided negligible coverage compared with the WAC dataset. Our mapping from MDIS uses all available WAC views of the north polar region to identify areas that are in shadow whenever imaged.

The majority of WAC images were acquired as part of MESSENGER's global mapping campaigns to create multiple monochrome and color base maps of the planet. Images were captured either as color sets or as individual monochrome images. The color sets were comprised of 3–11 images acquired with the narrow-band filters on the WAC filter wheel. Each individual image in a given color set was acquired 1–4 s after the previous one in the set, resulting in negligible changes in illumination and viewing conditions among images within a color set. To map regions of shadow, we used images taken with the 750-nm filter (5.1-nm bandwidth), which

was used in all of the global monochrome and color mapping campaigns. Since the other narrow-band WAC filters were always used in conjunction with the 750-nm filter, the images acquired with these other filters contain no information not captured by the 750-nm filter imaging. These 750-nm filter images capture the full range of illumination conditions available in the narrow-band WAC MDIS dataset. In total, 15,626 750-nm filter images centered at or poleward of 65°N were taken during MESSENGER's orbital operations.

In contrast, the MDIS 700-nm broadband filter (600-nm bandwidth) was utilized in a separate campaign to image within the shadowed regions near Mercury's north pole by scattered sunlight (Chabot et al., 2014). This WAC broadband filter was used to image the floors of north polar craters in an effort to observe the radar-bright deposits directly. This campaign resulted in a wide range of exposure times, given the trial-and-error approach of imaging the surfaces in permanent shadow. Although there are 3,270 WAC broadband filter images that fall within the area from 65°N to 90°N, the majority of these images by design contain substantial saturation, which leaked into shadowed portions of the image as an artifact of the goals of the campaign. Thus, for the WAC broadband images, we limited our dataset to the images with exposure times ≤2 ms that have fewer than 50 saturated pixels, resulting in 581 images.

In total, 16,207 WAC images taken with the narrow-band 750-nm filter and the broadband 700-nm filter were used to map areas of persistent shadow from 65°N to the pole (Fig. 1). The coverage is greater than that used in the previous study to map shadow in this area after one year of MESSENGER operations (Chabot et al., 2013). With this complete dataset, each surface point in the region, mapped at 200 m/pixel, was imaged on average 50 times. The most sampled locations were observed in over 220 images. The locations that were sampled the least, at the lowest latitudes and at some regions north of 85°N, have coverage from at least 9 images. The

narrow low-count edges on Fig. 1 are an artifact of our image selection process, namely that only images with a central latitude of 65°N or greater were considered.

Each of the 16,207 WAC images was map-projected at a pixel scale of 200 m in a polar stereographic projection, using an MLA-produced digital elevation model (DEM) for orthorectification. A photometric correction (Domingue et al., 2015) was applied to the 750-nm-filter images located at latitudes south of 84°N to produce more uniform surface-reflectance values. Images north of 84°N had high incidence angles that were challenging for the photometric correction, and surface coverage near the pole would have been lost if such a correction had been applied, so no photometric correction was applied to these images. No photometric correction has been developed for the WAC broadband filter images, so these images were also not photometrically corrected.

Each image was then divided into areas of illumination and shadow, automated by thresholding each image on the basis of the digital number value of individual pixels. By accounting for differences in viewing and lighting conditions with the photometric correction, a single threshold value could be used to classify all 750-nm filter images at latitudes south of 84°N into sunlit and shadowed terrain. A single lower threshold value was used for the higher-latitude 750-nm filter images without the photometric correction. The broadband filter images required yet another threshold value because of differences in the narrow-band and broadband passes. Numerous thresholding values were explored for each filter and for multiple latitudinal bins, but they did not change the general locations of shadowing. For example, threshold values that varied by 50% resulted in only a ~10% difference in the region mapped as shadowed, less than the ~25–30% change observed in the previous north polar (Chabot et al., 2013) and south

polar (Chabot et al., 2012) shadowing studies. Thus, keeping the approach simple by involving only three different thresholding values is appropriate for this dataset.

The thresholded images were combined onto a single map of Mercury's north polar region. As noted above, any area that remained in shadow in all of the images was classified as a region of "persistent shadow," meaning that the region was in shadow during all of the images acquired of that surface during MESSENGER's complete orbital mission. The images were acquired during a variety of local times and therefore reveal the surface under a range of illumination conditions. With such a robust dataset (Fig. 1), regions identified as "persistent shadow" become increasingly likely to be regions of permanent shadow. However, because it is possible that MESSENGER did not capture images of the north polar region under all illumination conditions, especially at the specific times of minimized shadow, the persistently shadowed regions mapped here may overestimate the regions of permanent shadow. Conversely, the accuracy of our mapped regions of persistent shadow is also limited by the registration of our imagery; imperfect pixel registration has the effect of decreasing the area mapped as persistently shadowed. Because we selected only those pixels that are shadowed in every image, if areas of shadow are misregistered between images, the shadowed pixels that do not overlap will be excluded in the shadow map. With these limitations, our map of persistent shadow is accurate in identifying shadowed regions in craters with diameters ≥6 km, as registration issues can be observed in smaller craters but larger shadowed craters are consistently identified, as discussed in more detail in section 4.3. The area of the host crater provides a maximum limit to the area of shadow, but most shadowed regions are only a fraction of the host crater in size. For example, the shadow in a 6-km-diameter crater typically takes up ~50% of the host crater's area northward of 80°N, although this statistic increases with latitude.

To analyze our shadow maps in context, we also generated an average mosaic of Mercury's north polar region from the same 750-nm filter dataset. The mosaic was created at a pixel scale of 200 m in a polar stereographic projection and registered with the same MLA-derived DEM as that used to produce the shadow map. The average mosaic is available in the supplementary material (Fig. S1).

2.2. Mapping Shadows from MLA Topographic Data

During MESSENGER's four years of orbital operations, MLA acquired more than 26 million altimetric range measurements of Mercury's surface, primarily in the northern hemisphere. An off-nadir campaign during the first extended mission was critical to the acquisition of topographic data poleward of 84°N. A crossover adjustment similar to that employed by Zuber et al. (2012) was performed on 3,186 selected MLA tracks to remove artifacts due to errors in spacecraft position knowledge and pointing and remaining noise. From this dataset, a DEM of Mercury's north polar region was constructed from MLA topographic data at a pixel scale of 500 m (Fig. 2). Despite some remaining coverage gaps at latitudes poleward of 84°N, this map can be used for modeling solar illumination conditions throughout the north polar region of Mercury. Elevation values were interpolated for areas where MLA data do not exist in the study region.

We followed the methodology of Mazarico et al. (2011) to compute solar illumination. First, the topographic map was used to compute the angular elevation of topographic obstacles in every azimuthal direction, for every pixel in the study region. These computations are more efficient when performed in gnomonic projection, allowable in the polar regions of the Moon and Mercury because of the low obliquities of these bodies, i.e., the Sun projects to near-infinity and

thus appears in the same "direction" for all the pixels on the map. We selected an azimuthal resolution of 1°, coarser than the 0.5° used by Mazarico et al. (2011), but sufficient given the larger apparent size of the Sun at Mercury (~1.14° at aphelion, compared with ~0.27° from the Moon). At every evaluation time step and for every pixel, the Sun's sky position was computed and its elevation compared with the horizon elevation, interpolated at the Sun's azimuthal position.

The position of the Sun in Mercury's body-fixed frame was computed following the SPICE toolkit (Acton et al., 1996) with the Mercury IAU reference frame (Margot, 2009; Archinal et al., 2011) and the JPL Solar System ephemerides (Folkner et al., 2014). The Sun was modeled as an extended source; its apparent radius, which varies with Mercury's eccentricity, was compared with the horizon's angular elevation in the appropriate azimuthal bins. Because of Mercury's eccentric orbit and 3:2 spin-orbit resonance, solar insolation varies with longitude: average insolation is less at longitudes 90°E and 270°E (Mercury's so-called "cold-pole" longitudes), resulting in temperatures as much as 130 K lower at the equator than at longitudes 0°E and 180°E (Mercury's "hot-pole" longitudes) (Vasavada et al., 1999). Because of the spin-orbit resonance, the maximum solar disc radius is larger near the hot-pole longitudes than near the cold-pole longitudes, potentially reducing those areas in permanent shadow that therefore qualify thermally as cold traps.

This method allowed us to simulate the illumination conditions at every hour over a long time period of 20 Mercury solar days, or ~9.6 Earth years. The illumination was computed as the portion of the Sun's solar disc area that fell above the linearly interpolated horizon. Our rectangular study region covers the latitudes 69°N–90°N entirely and extends down to 61°N near longitudes 45°E, 135°E, 225°E, and 315°E. We consider that pixels that were not illuminated

during our simulation period to be in permanent shadow; this assumption is justified because Mercury's obliquity is stabilized by the planet's spin-orbit resonance (Siegler et al., 2013) and has a very small value at <0.04°, much smaller than the Sun's angular radius (Margot, 2009). The thermal and illumination conditions in the polar regions are primarily controlled by Mercury's eccentricity, which is highly variable on timescales of 10 My (Siegler et al., 2013). Our simulations are based on Mercury's current orbital parameters, and thus what we determine as "permanent shadow" may not apply over such long timescales. We determined, however, that a change in eccentricity does not substantially change the modeled region of permanent shadow, as discussed in more detail in section 4.2. Only areas of modeled permanent shadow that were greater than one pixel in size were retained, as one-pixel areas may be artifacts resulting from limitations of the data or method.

3. Results

3.1. North Polar Shadow Maps

The MDIS- and MLA-derived shadow maps show strong agreement in the spatial distribution of shadows (Fig. 3). Full-resolution shadow maps at a pixel scale of 200 m are available in the supplemental material (Figs. S2, S3). The MDIS-derived map of areas of persistent shadow and the MLA-derived map of areas of permanent shadow both indicate that ~1.1% of the surface area between 65°N and 90°N is in steady shadow (Table 1). These values are similar to the ~1% that was calculated for the region between 65°N and 85°N from MDIS images after the first year of orbital data (Chabot et al., 2013). The percentage of persistently and

permanently shadowed terrain increases with latitude (Table 1; Fig. S4), as expected because of Mercury's low obliquity of only 2.04 arcmin (Margot et al., 2012). Thus solar illumination always strikes polar surfaces at extremely low angles, and some terrains and crater interiors never experience direct sunlight. With both methodologies, persistently and permanently shadowed regions can be identified equatorward to the lowest-latitude craters that host radar-bright deposits, including the 25-km-diameter Egonu crater at ~67.1°N, 61.6°E (Fig. 3), demonstrating that both methods are effective over the full north polar region.

As discussed, previous analysis of images from just one year of MESSENGER orbital data resulted in mapping gaps northward of ~86°N (Chabot et al., 2013). With the completion of the MESSENGER mission, not only are there substantially more images of the surface, but also complete coverage of Mercury's north polar region. We largely focus our discussion on the region from 80°N to 90°N to address the former data gap in the previous study and to investigate the region that contains the majority of the northern radar-bright deposits (Fig. S4). Our shadow maps show that, in the region from 80°N to 90°N, ~4.7% of the surface is persistently shadowed in the MDIS-derived map and ~5.8% is permanently shadowed in the MLA-derived map (Table 1). These values are similar to the ~4.5% and ~5.6% of permanently shadowed surface modeled for areas within 10° of latitude of the Moon's north and south poles, respectively (Mazarico et al., 2011). The relative surface area in persistent and permanent shadow increases with latitude: MIDS- and MLA-derived shadow maps show that ~13% and ~17%, respectively, of the surface between 85°N and 90°N is in persistent and permanent shadow. These values are below the ~20% of shadowing reported for a comparable region near Mercury's south pole (Chabot et al., 2012) and are higher than the ~6.6% and ~9.7% reported for the Moon's north and south polar regions, respectively (Mazarico et al., 2011).

Although similar to the MDIS-derived persistent shadow coverage, the amount of area mapped as permanent shadow in the MLA-derived map is consistently higher, as detailed in Table 1. In general, the MLA-derived shadow map identifies more permanently shadowed area at higher latitudes, especially from 86°N to the pole (Fig. 3, Fig. S4). Whereas some of this additional shadow may stem from limited coverage of MLA in this northern region, especially of the rims of large craters, much of this additional mapped shadow highlights small regions of permanent shadow within small craters and rough terrain that are beyond the resolution of the MDIS map. Imperfect registration between MDIS images prevents the detection of these small shadowed areas, less than a few kilometers across, as discussed in more detail in section 4.3.

Overall, there is strong agreement between the two shadow maps produced from the MDIS and MLA data; similarities and differences are discussed in the next sections. This agreement gives confidence to both approaches, as they are independent and based on fundamentally different datasets but yield the same general results.

3.2. Comparison with Radar Data

The radar image that was used for comparison with the shadow maps was a combination of the images presented by Harmon et al. (2011) as their Figures 3b and 4, hereafter termed radar images 1 and 2, respectively. Radar image 1 was constructed from a weighted sum of twelve groups of Arecibo S-band (12.6 cm wavelength) observations, acquired over a span of six years, to minimize radar-shadowing effects (Harmon et al., 2011). An area that is in radar shadow is shielded from radar illumination because of viewing geometry. Minimizing regions in radar shadow is desirable to enable observations over the largest spatial extent possible of radar-bright

material. Radar image 1, however, does not cover the entire region from 65°N to 90°N but rather covers fully from 83°N to the pole and only partially from 80°N to 83°N. We supplemented radar image 1 data with the larger-scale radar view provided by radar image 2 for regions not covered by the first image. Radar image 2 covers the entire north polar region southward to 65°N, but it was produced from two separate images, the first covering three observation groups and the second covering four, and thus it may be more limited by radar shadowing effects than radar image 1. The Arecibo images have a 1.5 km pixel scale, substantially larger than the 200-m pixel scale of our MIDS north polar mosaic and persistently shadowed map and the 500-m pixel scale of our MLA-derived permanently shadowed map. The lower radar resolution impacts the quality of the registration between our shadow maps and the radar images. The reported accuracy of the position of the Arecibo radar data is 1.5–3 km (Harmon et al., 2011).

To classify surfaces as radar-bright, noise must be removed from the Arecibo data. Using the standard deviation of the noise reported by Harmon et al. (2011) for radar images 1 and 2, we first set a threshold above the mean of three standard deviations of the noise. However, we found a number of small radar-bright pixels that did not correlate with the topographic or geologic features with this noise threshold. With a threshold of three standard deviations of the noise, ~1.4% of the surface from 65°N to 90°N was classified as radar-bright. In contrast, with a threshold of four standard deviations of the noise, the figure adopted by Harmon et al. (2011) to calculate the areal coverage of radar-bright material, there was much better agreement between the radar-bright regions and the surface topography, and we similarly chose to adopt this figure for our analysis. With a threshold of four-standard-deviations of the noise, the radar-bright material was seen to cover ~0.38% of the surface from 65°N to 90°N (Table 1), and the radar-bright area increases to ~2.2% from 80° to 90°N and to ~8.4% from 85° to 90°N (Fig. S4). A

comparison of radar maps with the two different noise thresholds is available in the supplemental material (Fig. S5).

The strong spatial agreement between areas in Mercury's north polar region with persistent and permanent shadow and radar-bright deposits is shown in Fig. 4. A total of ~79% of the area of radar-bright deposits between 80°N and 90°N coincides with areas of persistent shadow determined from images, and ~80% of the area of radar-bright deposits coincides with areas of permanent shadow determined from topography (Table 1). The percentage of radar-bright material that collocates with persistently and permanently shadowed areas is similar for the latitude bands 65°N–90°N, 80°N–90°N, and 85°N–90°N (Table 1). The remaining ~20% of radar-bright material is found either within 5 km of large areas of mapped persistent and permanent shadow or inside small craters with diameters ≤6 km, both situations attributable to limitations in the respective methodologies used with the MESSENGER and radar data.

Interestingly, in the region from 80°N to 90°N, only ~46% of the areas of persistent shadow determined from images and ~43% of the areas of permanent shadow derived from altimetry contain radar-bright materials, and these percentages are fairly consistent across latitudinal bins (Table 1). The additional shadow in the MLA-derived map accounts for the slightly lower percentage of MLA-derived shadowed area that coincides with radar-bright material. Some of these shadowed regions that lack radar-bright material occur as small isolated regions and may not be conducive to the thermal stability of water ice. However, in both the MDIS- and MLA-derived maps, there are other, larger shadowed regions that do not appear to host substantial radar-bright deposits, as can be seen in Fig. 4 for the craters Burke, Sapkota, and Yamada. It is possible that these craters and other persistently and permanently shadowed regions actually do not host water ice, or that they host water-ice deposits that are covered by thicker lag deposits

that mask radar returns from the underlying ice, or alternatively that they host water ice that was not detected by the Earth-based radar observations because of visibility or sensitivity limits (Fig. 5). These possibilities are discussed further in section 4.3.

4. Discussion

4.1. First Look at the "Diffuse Patch"

One specific region of interest is the "diffuse patch" of radar returns (Fig. 4a), first discussed by Harmon et al. (1994) and in more detail by Harmon et al. (2001). In the Arecibo radar images is a region of unresolved brightness concentrated northward of 88°N that was located on the night side of the planet at the time of the Mariner 10 encounters. This diffuse patch was unlike the other discrete radar-bright features that are concentrated within discrete spots within craters and have halos of non-radar-bright material that coincide with the crater rims. Harmon et al. (2001) proposed that the diffuse patch was a dense collection of small permanently shadowed regions in the ejecta blankets of north polar craters. The strong radar signature in this area has been repeatedly observed but has never been identified in a geological context because of limited MDIS image coverage of this area.

This large patch of radar-bright material coincides with a patchy area of persistent and permanent shadow (Fig. 6). On the basis of MESSENGER image coverage of this region, the diffuse patch is seen to occupy topographically rough terrain near three large craters. Our data support the interpretation that the diffuse patch is a dense collection of small volatile deposits residing in the secondary craters and shallow depressions within the portions closest to the pole

of the hummocky ejecta blankets from these craters (Harmon et al., 2001). The diffuse patch is located in a thermal environment different from those of the crater floors where the majority of radar-bright deposits are found, yet it still hosts radar-bright material that is generally collocated with regions of shadow.

This specific area also allows for a detailed comparison between the shadow maps derived from imagery and topography. The MDIS-derived map of areas of persistent shadow (Fig. 6c) mirrors the general circular shape of the diffuse patch's radar-bright deposits (Fig. 6b) and also shows more shadow in eastern portions of the patch, similar to the distribution of the radar-bright materials. The MDIS-derived map of areas of persistent shadow, however, misses the string of shadow to the south, reflecting the map's limitations that stem from image registration and possible sampling issues. In contrast, the MLA-derived map of areas of permanent shadow identifies this string of shadow to the south and also resolves many additional regions of permanent shadow that are missed in the MDIS-derived map of areas of persistent shadow as a result of registration issues (Fig. 6d). The MLA-derived map, however, does not capture the overall circular pattern of the diffuse patch or the larger concentration of shadow in the eastern portion of the patch. Overall, both shadow maps are similar on a global scale, but studies of specific areas show differences between the two approaches, demonstrating the strengths and limitations of each methodology, as illustrated by this example.

4.2. Shadow in Prokofiev

Prokofiev is a large, 112-km-diameter crater centered at ~85.8°N, 62.9°E (Fig. 3). Early radar studies identified a large radar-bright deposit in this region (Harmon et al., 1994, 2001),

and the deposit was later determined by MESSENGER to be located on the floor of Prokofiev in a crescent-shaped region of persistent shadow concentrated near the crater's steep north-facing wall (Chabot et al., 2013; Neumann et al., 2013). Prokofiev is of special interest because thermal studies indicate that water ice could survive over geological timescales even when exposed at the surface; this situation is in contrast to lower-latitude craters that host radar-bright deposits and for which models predict that any long-lived water ice must be buried beneath an insulating layer at least several tens of centimeters thick (Paige et al., 2013). MLA reflectance measurements at 1064 nm wavelength in Prokofiev's radar-bright region are higher than the surrounding terrain's average reflectance by about a factor of two (Neumann et al., 2013), and WAC broadband images reveal that the shadowed portion of Prokofiev's floor has a higher surface reflectance at visible wavelengths than the neighboring surface (Chabot et al., 2014). The higher reflectance values documented by MLA and MDIS have been interpreted as that of water ice exposed on the persistently shadowed portion of Prokofiev's floor. Similar extensive regions with high surface reflectance values have not been resolved by MLA or MDIS for any other shadowed crater on Mercury, though the four largest craters near Mercury's north pole (Chesterton, Kandinsky, Tolkien, and Tryggvadóttir) may also provide thermal environments conducive to long-lived surface water ice (Paige et al., 2013). MLA reflectivity measurements are inconclusive for these four craters in this most northern region because of the high emission angle of the observations, although observations of Kandinsky are suggestive of higher reflectance (Neumann et al., 2013). Reflectivity boundaries are also difficult to capture in MDIS images for these craters because the floors of these craters are completely in permanent shadow, so they do not have any sunlit terrain to provide a reflectivity comparison, as does Prokofiev.

We compare the spatial distribution of Prokofiev's radar-bright deposits with the areas of persistent or permanent shadow in Fig. 7. It is apparent that the two determinations of shadowed terrain, although generally similar, differ in their spatial extent. The MDIS-derived areas of persistent shadow (Fig. 7d) show close coincidence with the locations of radar-bright material (Fig. 7c), whereas the MLA-derived area of permanent shadow (Fig. 7e) is smaller. If the extent of the MLA-derived shadow is accurate, then some of Prokofiev's radar-bright deposits extend into regions that receive direct sunlight. However, Vasavada et al. (1999) concluded that it is not possible for ice deposits to survive for geologically long intervals in any sunlit region of Mercury's north polar region, whether such deposits are exposed on the surface or buried beneath an insulating layer. An alternative explanation of the differences in Fig. 7 is that the topographic data for Prokofiev's rim are not sufficiently comprehensive; a lower rim height in the DEM than actually present (e.g., as a result of interpolation in producing the DEM) could have yielded an illumination model that predicts too small a permanently shadowed region.

Because the areas of persistent shadow derived from MDIS images agree well with the distribution of radar-bright deposits in Prokofiev, it is tempting to conclude that the MDIS-derived map is correct. However, an intriguing offset exists between the boundaries of the radar-bright material and the high-reflectance surface inside Prokofiev that was observed in WAC broadband images (Chabot et al., 2014). In particular, the boundary of the area of high visible-wavelength reflectance is offset inward from that of the radar-bright region by ~3 km. This ~3 km offset is consistent with the smaller region of permanent shadow derived from MLA observations, as shown in Fig. 7d. If the MLA shadow map is unreliable in this region, then this agreement is just a coincidence. Alternatively, if the MLA-derived map of permanent shadow is more nearly correct, then rarely sunlit surfaces along the boundaries of permanently shadowed

areas may host stable subsurface water ice, accounting for the observed ~3 km offset. Vasavada et al. (1999) modeled idealized crater geometries, before Mercury's specific topography was known, and the available MLA data used by Paige et al. (2013) were too sparse and of too low a resolution to model insolation accurately. Further thermal modeling with the most complete topographic data available for Prokofiev is warranted.

To investigate further the differences between the MDIS-derived map of areas of persistent shadow and the MLA-derived model of areas of permanent shadow in Prokofiev, we focused on particular points along the observed offsets between the two predicted areas. From a catalogue of specific times when these points are predicted to be in sunlight by the MLA DEM, we searched for MDIS images that were captured near those times to establish whether the MLA topography has shortcomings, or instead there are gaps in MDIS sampling of local time of day. For points along the offset, illumination conditions were calculated for times throughout the MESSENGER mission, from March 2011 through April 2015, every 6 h. Figures 6a and 6b display two MDIS images used in this comparison, acquired 50 min and 119 min, respectively, after the time when the MLA model predicted that the points 85.057°N, 60.879°E and 85.067°N, 64.044°E, respectively, had been in sunlight. In both images, the points predicted to be in low sunlight (only a very small fraction of the solar disk is predicted to be visible) by the MLA model were in shadow, indicating that the MLA-derived model does not predict shadow accurately within Prokofiev at those locations and times. Additionally, the image used for this comparison in Fig. 7a was acquired with a long exposure, and the WAC broadband filter, and has high levels of saturation. Such an image was not used to generate the MDIS-derived shadow map but provides the best comparison for testing the MLA-derived predictions, as the long-exposure broadband images have high sensitivity to resolve surfaces even at low levels of sunlight. The MLA model

can underestimate the extent of shadow if measurements of the crater rims are not complete or accurate. Gaps in the MLA coverage and the required interpolation could result in a slightly inaccurate model of Prokofiev's rim elevation, leading to a predicted area of permanent shadow smaller than is actually the case (Fig. 7e).

It is important to note that the predicted areas of permanent shadow are based on current orbital parameters and that Mercury's orbital eccentricity can change these calculations. Differences in the calculations at high and low eccentricities, however, are expected to be larger at lower latitudes, with the largest changes along the hot-pole longitudes of Mercury. Mercury's eccentricity is variable even on timescales as short as ~10 My (Siegler et al., 2013), generally shorter than the geologic timescales invoked for discussions of water ice stability. We investigated the extent to which a change in eccentricity affects the calculation of the area of permanent shadow by creating two theoretical Mercury ephemerides with orbital eccentricities of 0.1 and 0.3, calculated extremes over the past 10 My (Siegler et al., 2013), for comparison with the current eccentricity of 0.206. The illumination simulation illustrates that an extreme end-member eccentricity value changes the area of permanent shadow but still results in an area smaller than that of radar-bright deposits (Fig. 7f). This comparison rules out eccentricity as a primary cause for the offset observed in Prokofiev between the boundaries of areas of high radar backscatter and MLA-derived areas of permanent shadow.

Thermal models for Mercury have used the MLA-derived DEM as input for calculations of insolation-derived heating (Paige et al., 2013). Such thermal models are only as accurate, of course, as the topography model used. If topography measurements are too sparse for the Prokofiev region at this level of detail, then the thermal models will be similarly affected and cannot be used to investigate the offset between the boundaries of the areas of high reflectance at

visible and radar wavelengths. Given the special data sets available for Prokofiev, further detailed thermal models of this region are warranted. Until such studies are completed, it is important to appreciate the potential limitations of thermal model results at this level of detail.

4.3. Distribution of Craters Hosting Radar-Bright Deposits

We examined the spatial relationship between our maps of areas of persistent and permanent shadow and images of radar-bright deposits on a crater-to-crater basis (Fig. 8). We cataloged all identifiable craters that are persistently shadowed on the MDIS-derived map (Table S1) and permanently shadowed on the MLA-derived map (Table S2) from 80°N to 90°N, and with the Small Body Mapping Tool (Kahn et al., 2011) we distinguished whether each crater hosts radar-bright material. The resolution of our average surface mosaic was limiting in the identification of small shadowed craters and may have prevented the identification of all such craters with diameters less than 5 km. When classifying craters as hosting or not hosting radar-bright material, it is worth noting that some craters coincide with locations of weak radar signatures that differ considerably from the stronger radar backscatter characteristic of many north polar craters. Craters were classified as radar-bright only when the area of high backscatter in the Arecibo image described in Section 3.2 covered at least 25% of the mapped area of persistent or permanent shadow. Thus, among craters that were classified as not hosting radar-bright materials, some may not be completely devoid of radar-bright material. Within 2° latitude of the pole, the low-incidence-angle illumination conditions made it impossible to identify all small craters <10 km in diameter, so mapping is likely incomplete at least in this region.

The craters identified as containing areas of persistent or permanent shadow are shown in map view in Figs. 7a and 7b and are classified as to whether they host radar-bright materials. Such a comparison allows us to seek patterns in the distributions of these populations and further examine the strengths and limitations of each shadow-mapping approach. Overall, 365 craters were mapped as persistently shadowed from the MDIS images, and 684 craters were mapped as permanently shadowed on the basis of the MLA-derived DEM. It is clear that the MLA-derived shadow map resolves smaller shadowed craters than the MDIS analysis, as the MDIS-derived shadow map is limited not only by the resolution of the images but also by the precision of registration between them.

Regions of shadow are distributed across the entire north polar region, present at all longitudes from 80°N to 90°N, as seen in Figs. 7c, 7d, and S4. These graphs also illustrate the size limitation of the two shadow-mapping methodologies. Although the MDIS-derived map identifies shadowed craters down to diameters as small as 1.8 km and the MLA-derived map down to 1.4 km, the agreement between the two approaches at these small sizes is poor. At crater diameters <4 km, the two maps identify only 29.9% of the same craters as shadowed. At diameters ≥4 km, the MDIS-derived shadow map identifies 85.2% of the craters hosting areas of permanent shadow in the MLA-derived map. This value increases to 98.8% for craters ≥5 km, with just one shadowed crater missing from the MDIS map, and the MDIS- and MLA-derived maps identify the same craters as shadowed for diameters ≥5.9 km. In the MLA-derived map, four craters that host radar-bright deposits, all <4 km in diameter, were not predicted to have areas in permanent shadow. The MDIS-derived map of areas of persistent shadow indicates as shadowed seven craters, all <5 km in diameter, that are not predicted to host areas of permanent shadow by the MLA DEM. In contrast, the MDIS-derived map of areas of persistent shadow

fails to resolve 62 craters, all with diameters <6 km, that host radar-bright deposits. Overall, all large radar-bright deposits within craters ≥6 km in diameter collocate with regions of shadow in both shadow maps. Thus, the two approaches to mapping shadow provide consistent and robust results for craters with diameters ≥6 km from 80°N to the pole.

From this mapping, we calculated the percentages of shadowed craters that do and do not host radar-bright deposits (Table 2). In the region from 80°N to 90°N, ~40% of the craters determined from MDIS images to be persistently shadowed and ~30% of the craters determined from topography to be permanently shadowed host radar-bright materials, figures similar to the ~46% and ~43% coverage of the respective areas of shadowed terrain that are reported as radar-bright (Table 1). These statistics are also consistent with the fact that the MLA-derived map identifies more small shadowed craters.

4.3.1. Distribution of Complex Craters Hosting Radar-Bright Deposits

From an examination of craters with diameters ≥10 km, a diameter that corresponds approximately to the size at which craters transition with increasing diameter from simple to complex morphologies on Mercury (Pike, 1988; Barnouin et al., 2012) and above which the MDIS- and MLA-derived catalogues of craters hosting shadowed areas show full agreement (Table 2), ~65% of shadowed craters host radar-bright deposits. Previous researchers have suggested that Mercury's shadowed cold traps may be fully occupied (Vasavada et al., 1999; Harmon et al., 2011; Chabot et al., 2013), yet our complete mapping work shows a considerable number of craters with shadowed areas that lack radar-bright deposits. These craters are at latitudes similar to those that host radar-bright deposits, suggesting that they create similar

thermal environments. That these cold traps are not occupied by water ice may thus indicate a lack of ice deposition rather than an unstable thermal environment (Fig. 5b).

Three large craters, Burke (centered at 85.9°N, 188.4°E), Sapkota (86.1°N, 227.2°E), and Yamada (82.5°N, 136.2°E), stand out for their absence of radar-bright deposits, even though their interiors are in nearly complete persistent or permanent shadow, as seen in Fig. 4. Additionally, these craters contain low-reflectance floor deposits, as measured by both MLA (Neumann et al., 2013) and MDIS imaging (Chabot et al., 2014), and such deposits have been interpreted within other craters to be surficial lag deposits that insulate underlying water ice. Calculations indicate that Burke, Sapkota, and Yamada have biannual maximum and average temperatures similar to those of surrounding craters that host radar-bright deposits (Paige et al., 2013). As noted above, it is possible that these craters host both water ice and surficial low-reflectance deposits that are unusually thick (Fig. 5c). A thickness for the surficial deposits of 2 m, for example, would attenuate an S-band return by 80% (Harmon et al., 2001). This thickness is substantially greater, however, than the 10–30 cm thickness inferred for the lag deposits insulating the majority of polar ice deposits on Mercury on the basis of the comparative variation of flux with latitude or epithermal and fast neutrons (Lawrence et al., 2013). It is possible that crater geometry can create an environment in which thicker lag deposits are more likely, especially if the crater is bowl-shaped with steeper walls. Some craters lacking radar-bright deposits are simple craters with steep slopes that are more conducive for the burial of ice. Differences in slope gradient could create a variety of thicknesses of the insulating deposit on top of the ice. If the ice is buried below a deposit thickened by downslope movement, this deposit would have to consist of low-reflectance material, because of the low-reflectance floor surface measured by both MLA (Neumann et al., 2013) and MDIS imaging (Chabot et al., 2014). Many

of the craters lacking radar-bright materials, however, are complex craters, and do not have a geometry where thick burial of ice is expected.

Another possibility is that these craters indeed host radar-bright deposits, but such deposits were not visible to the Earth-based radar during the times when radar data were collected at Arecibo. Lawrence et al. (2013), on the basis of MESSENGER NS results, concluded that the distribution of hydrogen in Mercury's north polar region is consistent with the hypothesis that radar-bright materials consist of water ice and inconsistent with a broad area of uniform hydrogen enrichment near the pole. However, Lawrence et al. (2013) also noted that the epithermal neutron flux data were consistent with, but did not require, a larger total area of water ice than that given by the known radar-bright regions, consistent with the possibility that permanently shadowed craters such as Burke, Sapkota, and Yamada host water-ice deposits that were not detected from Arecibo images. Such water-ice deposits may have been masked to radar imaging by anomalously thick lag deposits, as discussed above, be too thin to contribute to a strong radar return, or may not have been detected by the Earth-based radar observations because of visibility or sensitivity limits (Fig. 5d).

The longitudinal distribution of persistently and permanently shadowed craters can provide some insight into this possibility. As shown in Figs. 7c and 7d, the majority of shadowed craters with diameters ≥10 km host radar-bright deposits, but the fraction of shadowed craters that do not host radar-bright materials is higher near ~225°E than at other longitudes. These datasets are quantified in Table 2, where we show the percentage of craters from 80°N to 90°N that host radar-bright deposits for different longitudinal bins.

As discussed above, solar insolation varies with longitude because of Mercury's eccentric orbit and 3:2 spin-orbit resonance. The resulting longitudinal variation of surface and near-

surface temperatures serves to favor the retention of ice and other frozen volatiles at lower latitudes along the cold-pole longitudes (Harmon et al., 2001, 2007, 2011; Chabot et al., 2013). In the north polar region, south of 80°N, persistently shadowed craters hosting radar-bright materials show a strong preference for longitudes near 90°E and, to a lesser extent, 270°E (Chabot et al., 2013); a similar preference for radar-bright host craters north of 80°S was observed at Mercury's south pole (Chabot et al., 2012). In contrast to these results at lower latitudes, no correlation is observed between the percentage of shadowed craters that host radar-bright deposits and their locations relative to hot- and cold-pole longitudes from 80°N to 90°N, as shown in Table 2. For example, the cold-pole longitudes do not have the highest percentages of shadowed craters with radar-bright deposits; in the longitudinal bins from 45° to 135°E and from 225°E to 315°E, ~85% and ~70%, respectively, of the shadowed craters host radar-bright materials (Table 2). The bin from 315°E to 45°E, which includes Mercury's 0°E hot-pole longitude, contains the highest fraction of large, shadowed craters that host radar-bright materials (~93%). In contrast, the other hot-pole longitudinal bin from 135°E to 225°E contains the lowest fraction (~39%) of large, shadowed craters that host radar-bright materials. Moreover, the expected longitudinal variation of surface temperature on Mercury does not offer an explanation for the comparatively large fraction of shadowed craters that lack radar-bright deposits centered near 225°E.

We also compared the geologic characteristics of the shadowed regions that do and do not host radar-bright materials, including geologic units, surface roughness, and elevation, but no evident relations were found. For geologic units, we referenced the geologic map of the Borealis quadrangle of Mercury (Grolier and Boyce, 1984), a map produced from Mariner 10 data for which the majority of the north polar region from 65°N to 90°N was not mapped because of

coverage gaps and the similar local times of the flybys. The comparatively large number of shadowed craters that do not host radar-bright materials near ~225°E are in an area mapped as intercrater plains, a unit defined by hummocky, pitted, locally grooved and lineated plains (Grolier and Boyce, 1984) and older than intermediate plains and still younger smooth plains (Denevi et al., 2013). From a comparison with topographic roughness maps (Kreslavsky et al., 2014), which are limited to the latitudinal range 65°N to 84°N, most large (≥10 km in diameter), shadowed craters that lack radar-bright deposits are found in regions of rougher terrain, in agreement with the geologic mapping. But some craters, including Burke, Sapkota, and Yamada discussed above, are mapped in smooth plains, characterized by flat to gently rolling terrain (Grolier and Boyce, 1984). Thus, large, shadowed craters that lack radar-bright deposits span different geologic units and are not restricted to terrain of a certain age. The large, shadowed craters that lack radar-bright deposits do appear to correlate with regions of higher elevation. Although elevation may contribute to the extent of regions lying in permanent shadow, temperature models for large, shadowed craters (Paige et al., 2013) do not vary substantially with elevation over the range applicable here.

Next, we examined four longitudinal bins, each 90° in width, that should represent similar average thermal environments (i.e., each quadrant captures equal contributions from cold-pole and hot-pole longitudes). The percentage of shadowed craters that host radar-bright materials is uneven among these quadrants. More shadowed craters host radar-bright materials from 0°E to 90°E (Table 2), and the percentage of shadowed craters hosting radar-bright deposits is lowest in the quadrant from 180°E to 270°E, a range that includes the longitudes near 225°E mentioned above. Given that thermal environment does not appear to be the primary control on the percentage of shadowed craters that host radar-bright deposits, the distribution of radar-bright

deposits may be the result of uneven sampling by Earth-based radar imaging, possibly caused by viewing geometry restrictions or sensitivity issues during the radar observations. The radar image used for comparison was produced from a combination of Arecibo observations acquired during 12 discrete viewing opportunities; the sub-Earth positions of those images span the full range of Mercury longitudes, with a largest longitudinal gap of only 40° (Harmon et al., 2011). This good longitudinal coverage does not provide a simple explanation for the large number of shadowed craters that lack radar-bright material near 225°E.

To fully address this issue, the geometries of the ground-based radar observations were modeled using the Mercury topography measured by MLA, following the method described in Section 2.2 and expanding on a study by Mazarico et al. (2014). The radar data do not appear to suffer from any large gaps in coverage. Although the simulations identified small portions of crater floors as radar-invisible (Fig. S6), their combined area is only ~2400 km^2. The floors of Burke and Sapkota were visible to Earth-based radar for several of the observations of Harmon et al. (2011). Figure 9 shows both reconstructed viewing geometry and Earth-based radar data. The expected radar signal strength for these two craters from the Earth-Mercury distance was calculated (Fig. 9a–c) from the viewing geometry for three of the images of Harmon et al. (2011). A value of 100% would be achieved if the surface of Mercury were perpendicular to the line of sight. There were portions of the floors of Burke and Sapkota that were radar-invisible during these specific Earth-based observations, but there were also large portions of the craters that were visible to the radar (Fig. 9a–b).

We also compare in Fig. 9d–f the radar signal strength obtained during two individual acquisitions (Fig. 2 of Harmon et al., 2011) and over multiple observations (radar image 2 discussed in section 3.2). Areas with a ratio of radar signal strength to the acquisition root-mean-

square deviation is ≥ 4, as recommended by Harmon et al. (2011), are highlighted in red and are the "radar-bright" material. In Fig. 9d, a portion of Burke's floor has a radar-bright signature, at the threshold of four standard deviations of the noise, and a very small portion of Sapkota's floor shows a radar-bright signature. The area covered by radar-bright material decreases in Fig. 9e, which was constructed from a different Arecibo observation. In Fig. 9c, only a small percentage of Burke's floor has a radar-bright signature, and Sapkota's floor is completely devoid of any radar-bright signature at the given threshold level. Fig. 9f illustrates the effects of averaging over multiple radar observations. Burke crater, for example, may host some radar-bright material, but because it does not have a significant signal in all radar observations, its signal level decreased in the averaged radar image 2 that Harmon et al. (2011) constructed for the north polar region. Even though Burke did not have a strong return in all 12 observations, Burke may not have been visible in all of those observations (Fig. 9c). Times of radar invisibility, however, were not compensated in the averaged image. A loss of signal is also evident in small (< 10 km in diameter) craters that host radar-bright materials, as seen with craters A and B (Fig. 9). In summary, Burke and Sapkota show radar returns in individual observations. However, even when these two craters were visible in specific radar observations, they lack an extensive, concentrated signal that is typical of other persistently or permanently shadowed craters in the north polar region.

Overall, if visibility, sensitivity, or other factors have limited the radar images acquired to date, then the possibility that all of Mercury's cold traps in the north polar region are occupied remains open, consistent with the idea that either the water ice is geologically young or a regular refreshing mechanism exists. If sampling of the polar regions by radar imaging has not been restricted, in contrast, then the distribution of radar-bright materials may provide clues into the

source, history, or mobility of the water ice in this region by processes other than simple thermal equilibrium.

4.3.2. Distribution of Simple Craters Hosting Radar-Bright Deposits

Previous thermal models predicted that idealized simple bowl-shaped craters with diameters <10 km are not thermally stable environments for long-lived water-ice deposits, even with an insulating overlying layer, unless within 2° latitude of Mercury's poles (Vasavada et al., 1999). Our work shows that both the MDIS- and MLA-derived maps identify many small craters <10 km in diameter that are both shadowed and contain radar-bright deposits, as shown in Fig. 8 and quantified in Table 2. Previous studies (Harmon et al., 2001, 2011; Chabot et al., 2012, 2013), in addition to the work presented here, have shown that many radar-bright deposits lie within craters <10 km in diameter at latitudes farther equatorward than 88°N. Overall, for craters <10 km in diameter located between 80°N and the pole, ~35% of the persistently shadowed craters indicated by imaging and ~26% of the permanently shadowed craters indicated by topography host radar-bright materials (Table 2).

The majority of small (<10 km in diameter) craters that host radar-bright deposits are located between about 0°E and 90°E. A total of 64% of the small craters indicated from imaging to have areas of persistent shadow that host radar-bright materials and 73% of the craters indicated from topography to have areas of permanent shadow that host radar-bright materials are centered between 0°E and 90°E (Table 2). The higher percentages in this sector may be influenced by the large number of secondary craters from Prokofiev in this region. Prior to the return of MESSENGER data, idealized simple craters were modeled with a depth-to-diameter ratio of 1:5

(Vasavada et al., 1999), but MLA topographic measurements reveal that simple craters on Mercury are shallower than previously modeled (Ernst et al., 2014). Additionally, secondary craters are often shallower than primary craters of the same diameter (McEwen and Bierhaus, 2006). Shallower craters may provide a thermal environment that enables lower temperatures and allows water ice to be stable within these small, shadowed craters on geologic timescales. Detailed thermal modeling using measured topography for these small craters is needed to address this issue. If such modeling does not markedly change the results of Vasavada et al. (1999), then the water ice that constitutes the radar-bright material in these small craters must be geologically young, less than 1 Gy in age (Ernst et al., 2014).

The distribution of small craters with areas of persistent or permanent shadow also shows no relation to Mercury's cold- and hot-pole longitudes between 80°N and 90°N. The longitudinal bin from 315°E to 45°E capturing Mercury's 0°E hot-pole longitude and the bin from 45°E to 135°E capturing Mercury's 90°E cold-pole longitude show similar statistics: ~52% and ~54% of the small craters with persistently shadowed areas host radar-bright materials in these bins, respectively. Similarly, ~38% and ~41% of the small craters with permanently shadowed areas host radar-bright materials in these bins. The longitudinal bins that include Mercury's hot-pole longitude of 180°E and cold-pole longitude of 270°E also show similar statistics to one another. From 135°E to 225°E, ~14% and ~7.8% of small craters with persistently and permanently shadowed areas host radar-bright materials, respectively, similar to the ~14% and ~6.2% figures for the bin from 225°E to 315°E. These calculations reinforce the suggestions above that radar visibility or sensitivity may have limited the coverage of the Arecibo radar images, especially near ~225°E, or that water ice is less abundant or buried under thicker deposits in this general region.

5. Conclusions

Determining the regions of permanent shadow near Mercury's north pole is key to constraining the areas in which water ice may persist on Mercury over geologically long intervals. A comparison of the spatial distribution of regions of permanent shadow to that of high radar backscatter in Earth-based radar images has important implications for radar-bright materials on Mercury:

(1) Produced with two independent methods and different datasets, maps of areas of persistent shadow determined from MDIS images and of areas of permanent shadow from an MLA-derived digital elevation model show strong agreement over the entire north polar region, from 65°N to 90°N. In particular, both approaches produce consistent catalogues of shadowed craters with diameters ≥6 km from 80°N to the pole.

(2) Some differences between the maps of shadowed areas are seen. In Prokofiev crater, for instance, the area of permanent shadow is likely underestimated on the basis of a comparison with shadowed areas in images. More extensive measurements of Prokofiev's topography, especially along its rim, should help to resolve the observed differences. The MLA-derived maps of areas of permanent shadow do, however, successfully capture craters with partially shadowed interiors at smaller diameters than the approach with MDIS images.

(3) Earth-based observations of radar-bright features coincide with regions of persistent or permanent shadow in Mercury's north polar region, confirming previous work. Specifically, all large radar-bright deposits within craters ≥6 km in diameter collocate with regions of persistent

and permanent shadow derived from the MDIS and MLA datasets. This result is consistent with the conclusion that the radar-bright material on Mercury consists dominantly of water ice.

(4) Many areas of persistent or permanent shadow determined from the MDIS and MLA datasets lack radar-bright deposits, including the interiors of a number of impact craters ≥10 km in diameter. If there is no water ice in these regions, then not all of Mercury's cold-traps are occupied. Alternatively, it is possible that the water ice is present in such areas but is masked to radar imaging by anomalously thick lag deposits or is too thin to contribute to a strong radar return. There is a longitudinal dependence of the locations of large (≥ 10 km in diameter) craters with areas of persistent or permanent shadow that lack radar-bright deposits. This dependence is not controlled by the longitudes of Mercury's hot and cold poles, however. If water ice is present in these shadowed craters but measurements were limited by radar visibility or sensitivity, then water ice may occupy all available cold traps near Mercury's north polar region.

(5) Although most small (<10 km in diameter) simple craters do not host radar-bright deposits, many small craters near the 112-km-diameter crater Prokofiev do host such deposits. Most of the latter craters are secondary craters from Prokofiev and may be shallower than primary craters of the same diameter. Additional modeling of the thermal environment of Mercury's simple craters with measured topography is warranted, given the large number of such craters observed to host radar-bright materials.

Acknowledgments

We thank David Lawrence for helpful discussions about this work, Oded Aharonson for smooth editorial handling of the manuscript, and Matt Siegler and an anonymous reviewer for constructive comments that improved the final paper. The MESSENGER project is supported by

the NASA Discovery Program under contracts NAS5-97271 to The Johns Hopkins University Applied Physics Laboratory and NASW-00002 to the Carnegie Institution of Washington. Support was also provided by NASA Discovery Data Analysis Program grant NNX15AK89G. This research has made use of the Small Body Mapping Tool of The Johns Hopkins University Applied Physics Laboratory and the Integrated Software for Imagers and Spectrometers of the U.S. Geological Survey. All data analyzed in this paper are archived at the NASA Planetary Data System.

References

Acton, C.H., 1996. Ancillary data services of NASA's navigation and ancillary information facility. Planet. Space Sci. 44, 65–70. http://dx.doi.org/10.1016/0032-0633(95)00107-7.

Archinal, B.A., et al., 2011. Report of the IAU Working Group on Cartographic Coordinates and Rotational Elements: 2009. Celest. Mech. Dyn. Astron. 109, 101–135. http://dx.doi.org/10.1007/s10569-010-9320-4.

Barnouin, O.S., et al., 2012. The morphology of craters on Mercury: Results from MESSENGER flybys. Icarus 219, 414–427. http://dx.doi.org/10.1016/j.icarus.2012.02.029.

Butler B.J., Muhleman, D.O., Slade, M.A., 1993. Mercury: Full-disk radar images and the detection and stability of ice at the north pole. J. Geophys. Res. 98, 15003–15023. http://dx.doi.org/10.1029/93JE01581.

Cavanaugh, J.F., et al., 2007. The Mercury Laser Altimeter instrument for the MESSENGER mission. Space Sci. Rev. 131, 451–479. http://dx.doi.org/10.1007/978-0-387-77214-1_13.

Chabot, N.L., et al., 2012. Areas of permanent shadow in Mercury's south polar region ascertained by MESSENGER orbital imaging. Geophys. Res. Lett. 39, L09204. http://dx.doi.org/10.1029/2012GL051526.

Chabot, N.L., et al., 2013. Craters hosting radar-bright deposits in Mercury's north polar region: Areas of persistent shadow determined from MESSENGER images. J. Geophys. Res. Planets 118, 26–36. http://dx.doi.org/10.1029/2012JE004172.

Chabot, N.L., et al., 2014. Images of surface volatiles in Mercury's polar craters acquired by the MESSENGER spacecraft. Geology 42, 1051–1054. http://dx.doi.org/10.1130/G35916.1.

Denevi, B.W., et al., 2013. The distribution and origin of smooth plains on Mercury. J. Geophys. Res. Planets 118, 891–907. http://dx.doi.org/10.1002/jgre.20075.

Domingue, D.L., Denevi, B.W., Murchie, S.L., Hash, C.D., 2015. Characterization of Mercury's regolith with multiple photometric models. Lunar Planet. Sci. 45. Abstract 1341.

Ernst C.M., Chabot, N.L., Susorney, H.C.M., Barnouin, O.S., Harmon, J.K., Paige, D.A., 2014. Exploring the morphology of simple craters that host polar deposits on Mercury: Implications for the source and stability of water ice. Lunar Planet. Sci. 45. Abstract 1238.

Folkner, W.M., Williams, J.G., Boggs, D.H., Park, R.S., Kuchynka, P., 2014. The Planetary and Lunar Ephemerides DE430 and DE431. Interplanetary Network Progress Report 42-196, Jet Propulsion Laboratory, Pasadena, Calif.

Grolier, M.J., Boyce, J.M., 1984. Geologic map of the Borealis Region (H-1) of Mercury. Map I-1660, Misc. Investigations Ser., U.S. Geological Survey, Denver, Colo.

Harmon, J.K., 2007. Radar imaging of Mercury. Space Sci. Rev. 132, 307–349. http://dx.doi.org/10.1007/s11214-007-9234-y.

Harmon, J.K., Slade, M.A., 1992. Radar mapping of Mercury: Full-disk images and polar anomalies. Science 23, 640–643. http://dx.doi.org/10.1126/science.258.5082.640.

Harmon, J.K., Slade, M.A., Velez, R.A., Crespo, A., Dryer, M.J., Johnson, J.M., 1994. Radar mapping of Mercury's polar anomalies. Nature 369, 213–215. http://dx.doi.org/10.1038/369213a0.

Harmon, J.K., Perillat, P.J., Slade, M.A., 2001. High-resolution radar imaging of Mercury's north pole. Icarus 149, 1–15. http://dx.doi.org/10.1006/icar.2000.6544.

Harmon, J.K., Slade, M.A., Rice, M.S., 2011. Radar imagery of Mercury's putative polar ice: 1999–2005 Arecibo results. Icarus 211, 37–50. http://dx.doi.org/10.1016/j.icarus.2010.08.007.

Hawkins III, S.E., et al., 2007. The Mercury Dual Imaging System on the MESSENGER spacecraft. Space Sci. Rev. 131, 247–338. http://dx.doi.org/10.1007 /s11214-007-9266-3.

Kahn, E.G., et al., 2011. A tool for the visualization of small body data. Lunar Planet. Sci. 42. Abstract 1618.

Kreslavsky, M.A., Head, J.W., Neumann, G.A., Zuber, M.T., Smith, D.E., 2014. Kilometer-scale topographic roughness of Mercury: Correlation with geologic features and units. Geophys. Res. Lett. 41, 8245–8251. http://dx.doi.org/10.1002/2014gl062162.

Lawrence, D.J., et al., 2013. Evidence for water ice near Mercury's north pole from MESSENGER Neutron Spectrometer measurements. Science 339, 292–296. http://dx.doi.org/10.1126/science.1229953.

Margot, J., 2009. A Mercury orientation model including non-zero obliquity and librations. Celest. Mech. Dyn. Astron. 105, 329–336. http://dx.doi.org/10.1007/s10569-009-9234-1.

Margot, J., et al., 2012. Mercury's moment of inertia from spin and gravity data. J. Geophys. Res. 117, E00L09. http://dx.doi.org/10.1029/2012JE004161.

Mazarico, E., Neumann, G.A., Smith, D.E., Zuber, M.T., Torrence, M.H., 2011. Illumination conditions of the lunar polar regions using LOLA topography. Icarus 211, 1066–1081. http://dx.doi.org/10.1016/j.icarus.2010.10.030.

Mazarico E., Nicholas, J.B., Neumann, G.A., Smith, D.E., Zuber, M.T., 2014. Illumination conditions at the poles of the Moon and Mercury, and application to data analysis. Lunar Planet. Sci. 45. Abstract 1867.

McEwen, A.S., Bierhaus, E.B., 2006. The importance of secondary cratering to age constraints on planetary surfaces. Annu. Rev. Earth Planet. Sci. 34, 535–567. http://dx.doi.org/10.1146/annurev.earth.34.031405.125018.

Neumann, G.A., et al., 2013. Bright and dark polar deposits on Mercury: Evidence for surface volatiles. Science 339, 296–300. http://dx.doi.org/10.1126/science.1229764.

Paige, D.A., Wood, S.E., Vasavada, A.R., 1992. The thermal stability of water ice at the poles of Mercury. Science 258, 643–646. http://dx.doi.org/10.1126/science.258.5082.643.

Paige, D.A., et al., 2013. Thermal stability of volatiles in the north polar region of Mercury. Science 339, 300–303. http://dx.doi.org/10.1126/science.1231106.

Pike, R.J., 1988. Geomorphology of impact craters on Mercury. In: Vilas, F., Chapman, C.R., Matthews, M.S. (Eds.), Mercury. University of Arizona Press, Tucson, Ariz., pp. 165–273.

Siegler, M.A., Bills, B.G., Paige, D.A., 2013. Orbital eccentricity driven temperature variation at Mercury's poles. J. Geophys. Res. Planets 118, 930–937. http://dx.doi.org/10.1002/jgre.20070.

Slade, M.A., Butler, B.J., Muhleman, D.O., 1992. Mercury radar imaging: Evidence for polar ice. Science 258, 635–640. http://dx.doi.org/10.1126 /science.258.5082.635.

Solomon, S.C., McNutt Jr., R.L., Gold, R.E., Domingue, D.L., 2007. MESSENGER mission overview. Space Sci. Rev. 131, 3–39. http://dx.doi.org/10.1007/s11214-007-9247-6.

Vasavada, A.R., Paige, D.A., Wood, S.E., 1999. Near-surface temperatures on Mercury and the Moon and the stability of polar ice deposits. Icarus 141, 179–193. http://dx.doi.org/10.1006/icar.1999.6175.

Zuber, M.T., et al., 2012. Constraints on the volatile distribution within Shackleton crater at the lunar south pole. Nature 486, 378–381. http://dx.doi.org/10.1038/nature11216.

Figure Captions

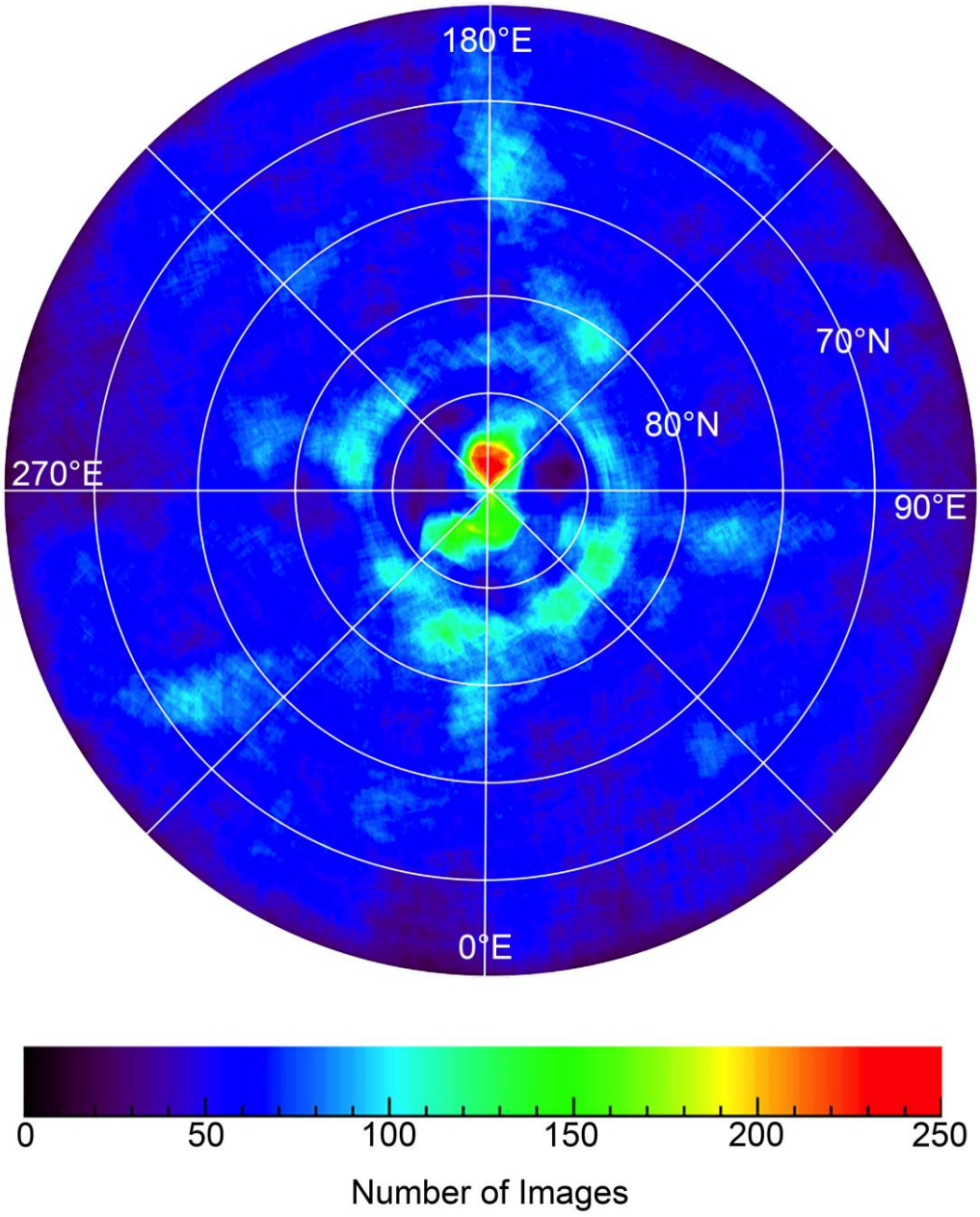

Fig. 1. Distribution of the number of WAC images centered at latitudes between 65°N and 90°N that were used to create the MDIS-derived map of areas of persistent shadow. On average, 50 images were used for each point on the surface, mapped at 200 m/pixel. A minimum of nine images was used for each surface point. Polar stereographic projection.

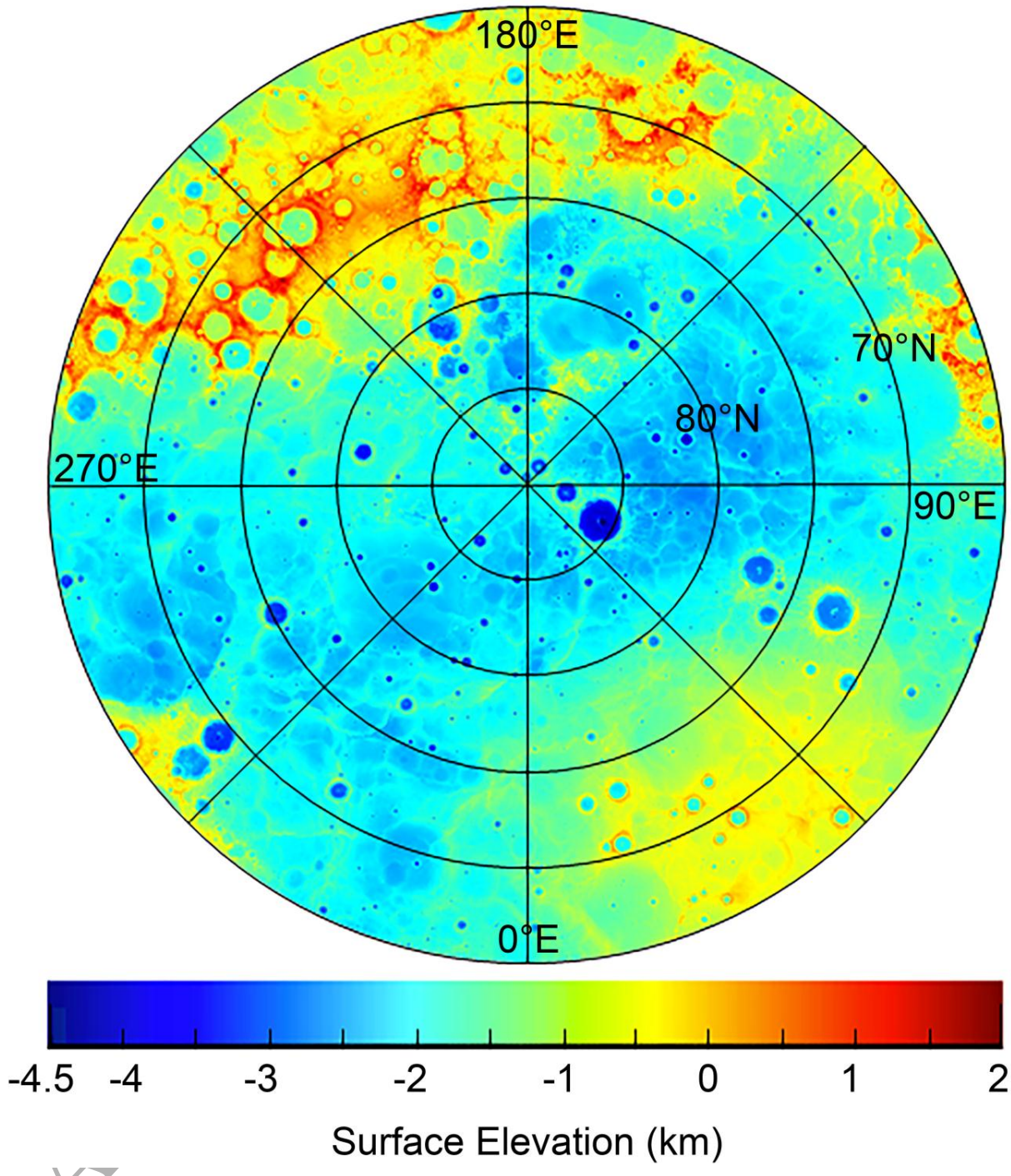

Fig. 2. Contour map of the digital elevation model derived from topographic data at latitudes between 65°N and 90°N that was used to create the MLA-derived map of areas of permanent shadow. The DEM has a pixel scale of 500 m. Polar stereographic projection..

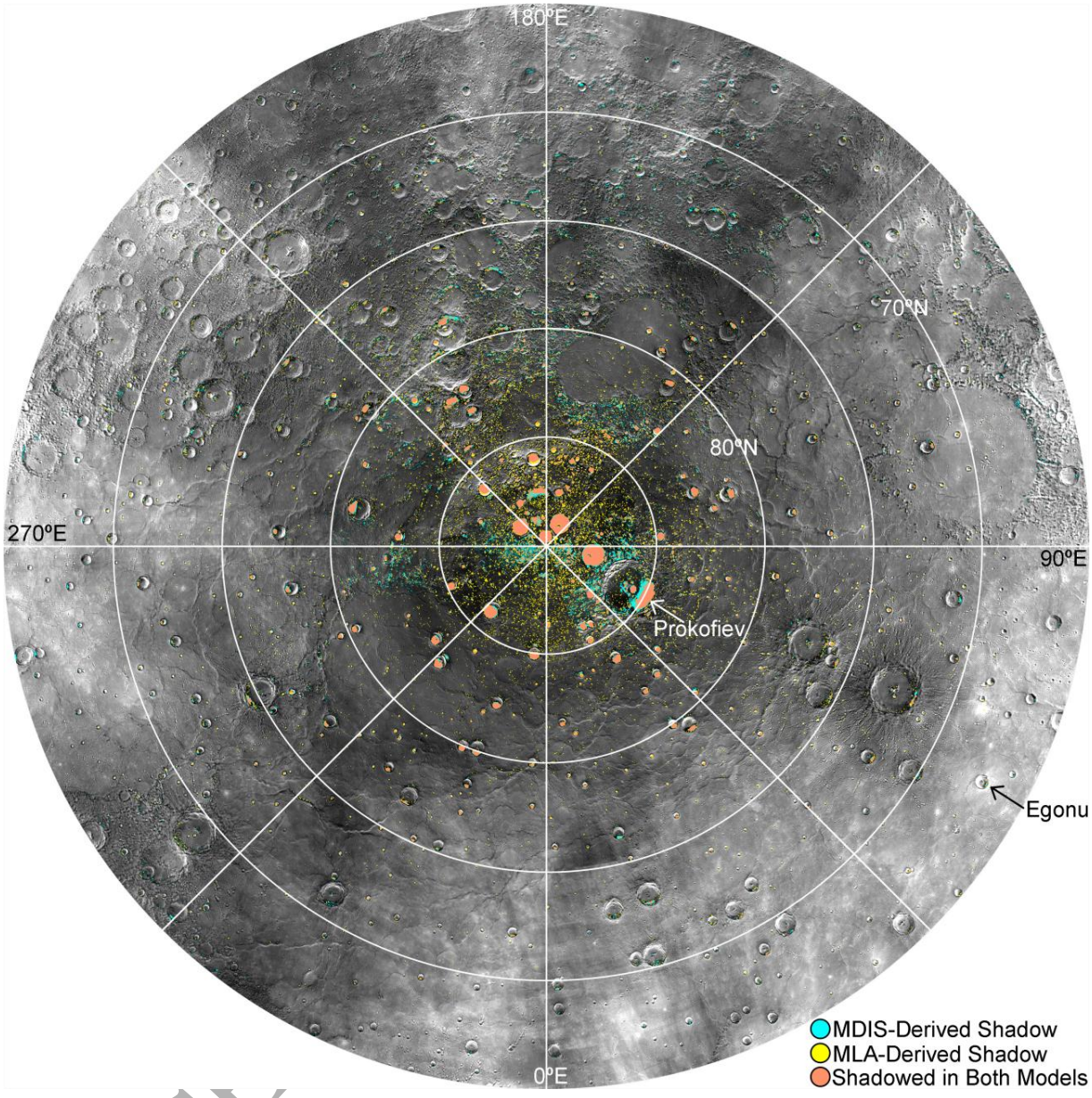

Fig. 3. Shadowed regions displayed on a mosaic of MESSENGER images from 65°N to 90°N in polar stereographic projection. Areas shadowed in all MDIS images of a given region are shown in cyan, areas shadowed in the MLA model are shown in yellow, and areas shadowed in both datasets are shown in coral. Prokofiev and Egonu craters are labeled.

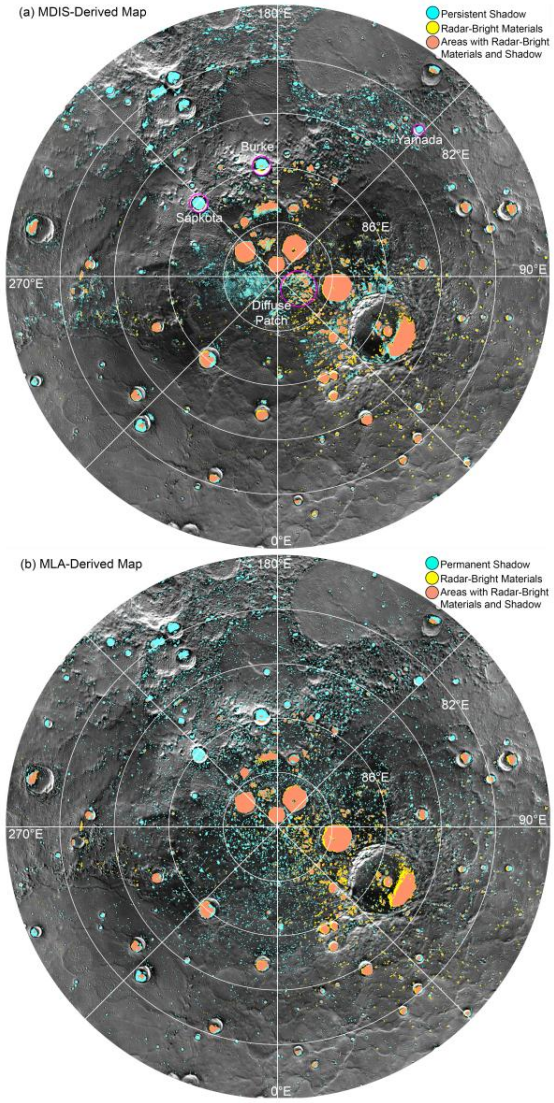

Fig. 4. Shadowed regions displayed on a mosaic of MESSENGER images from 80°N to 90°N in polar stereographic projection. (a) Areas shadowed in all MDIS images are shown in cyan, radar-bright deposits are in yellow, and areas with both shadow and radar-bright materials are in coral. The "diffuse patch," Sapkota, Burke, and Yamada craters are outlined in magenta. (b) Areas shadowed in the MLA model are shown in cyan, radar-bright deposits are in yellow, and areas with both shadow and radar-bright materials are in coral. Radar data are from Harmon et al. (2011).

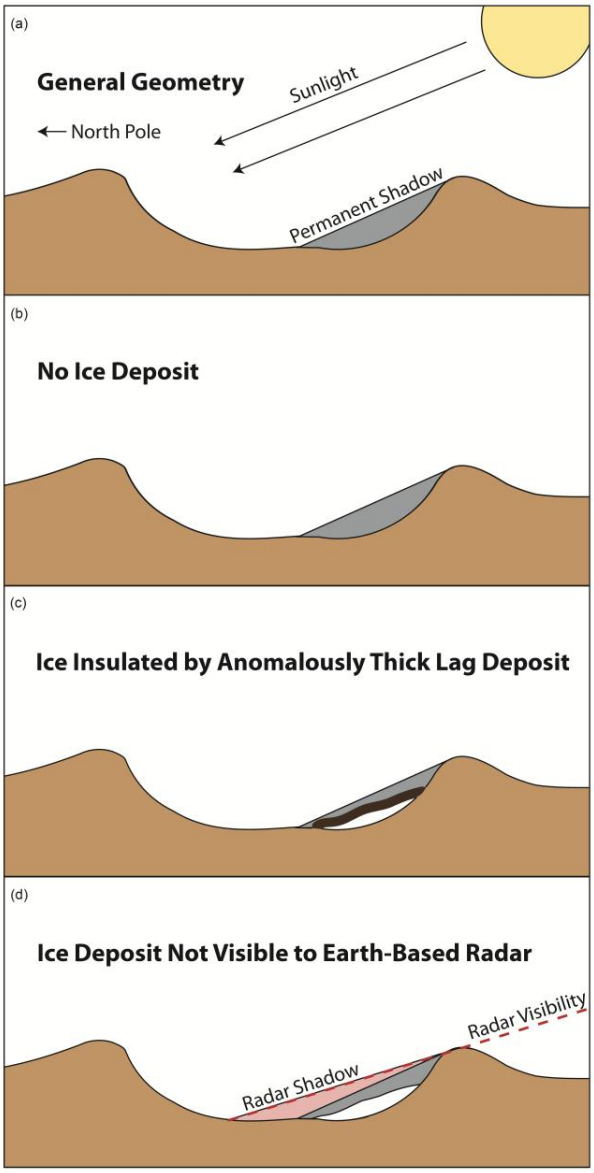

Fig. 5. (a) Schematic cross-section of a typical flat-floored crater near Mercury's north pole. A portion of the north-facing slope is in permanent shadow. For a persistently or permanently shadowed portion of a crater interior that lacks radar-bright deposits, there are three possibilities: (b) the crater interior does not host water ice, (c) the crater hosts water-ice deposits that are covered by lag deposits sufficiently thick that they mask radar returns from the underlying ice, or (d) the crater hosts water ice that was not detected by the Earth-based radar observations because of visibility or sensitivity limits.

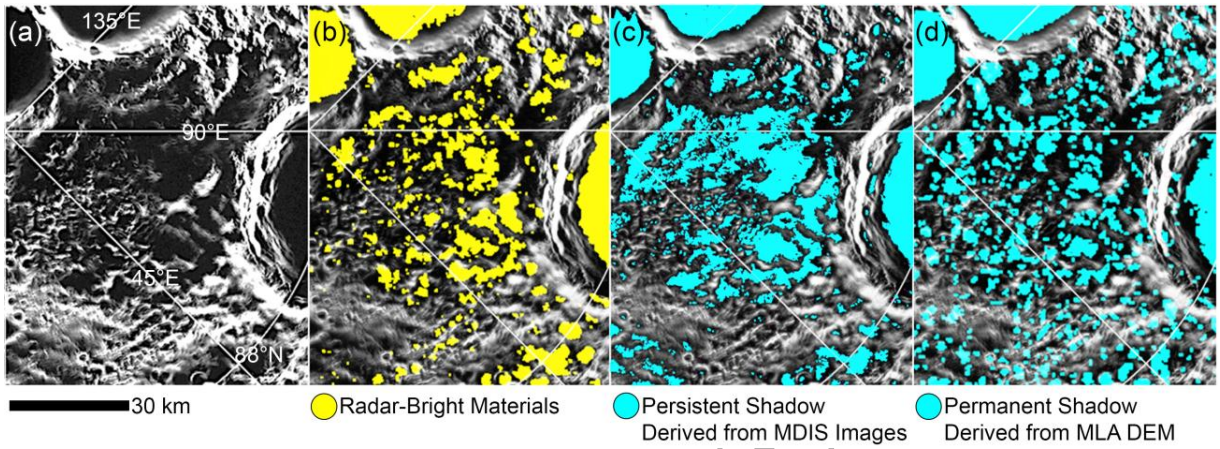

Fig. 6. (a) The "diffuse patch" seen in Earth-based radar images and centered at ~89.1°N, 60.5°E, shown on a mosaic of MESSENGER images in polar stereographic projection. (b) Regions with radar-bright materials are shown in yellow (Harmon et al., 2011). (c) Areas shadowed (cyan) in all MDIS images of a given region. (d) Areas permanently shadowed (cyan) in the MLA DEM.

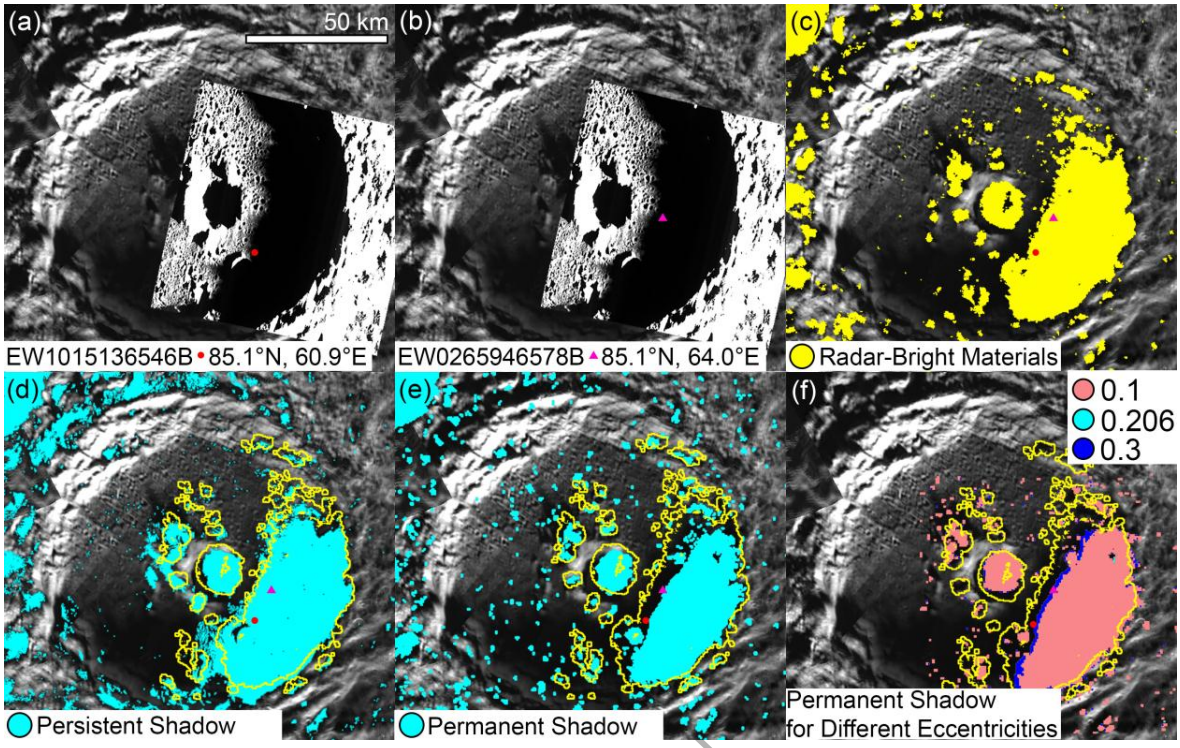

Fig. 7. Mosaic of MESSENGER images of Prokofiev, shown in polar stereographic projection. (a) MDIS image EW1015136546B is overlain on the mosaic; a red circle marks a point (85.067°N, 64.044°E) that is predicted to be in sunlight in the MLA-derived DEM at the specific time this image was acquired. (b) MDIS image EW0265946578B is overlain on the mosaic; a magenta triangle marks a point (85.057°N, 60.879°E) predicted to be in sunlight in the MLA-derived DEM at the specific time this image was acquired. The circle and triangle also appear in all later panels. (c) Regions of high radar backscatter are shown in yellow (Harmon et al., 2011). (d) Areas of persistent shadow (cyan) indicated in MDIS images; the largest radar-bright region in Prokofiev is outlined in yellow. (e) Areas predicted to be in permanent shadow (cyan) by the MLA-derived DEM. (f) Areas predicted to be in permanent shadows for different values of Mercury's orbital eccentricity. The area of shadow resulting from Mercury's current eccentricity (0.206) is in cyan but is hidden by those for eccentricity end-member values of 0.1 (coral) and 0.3 (blue).

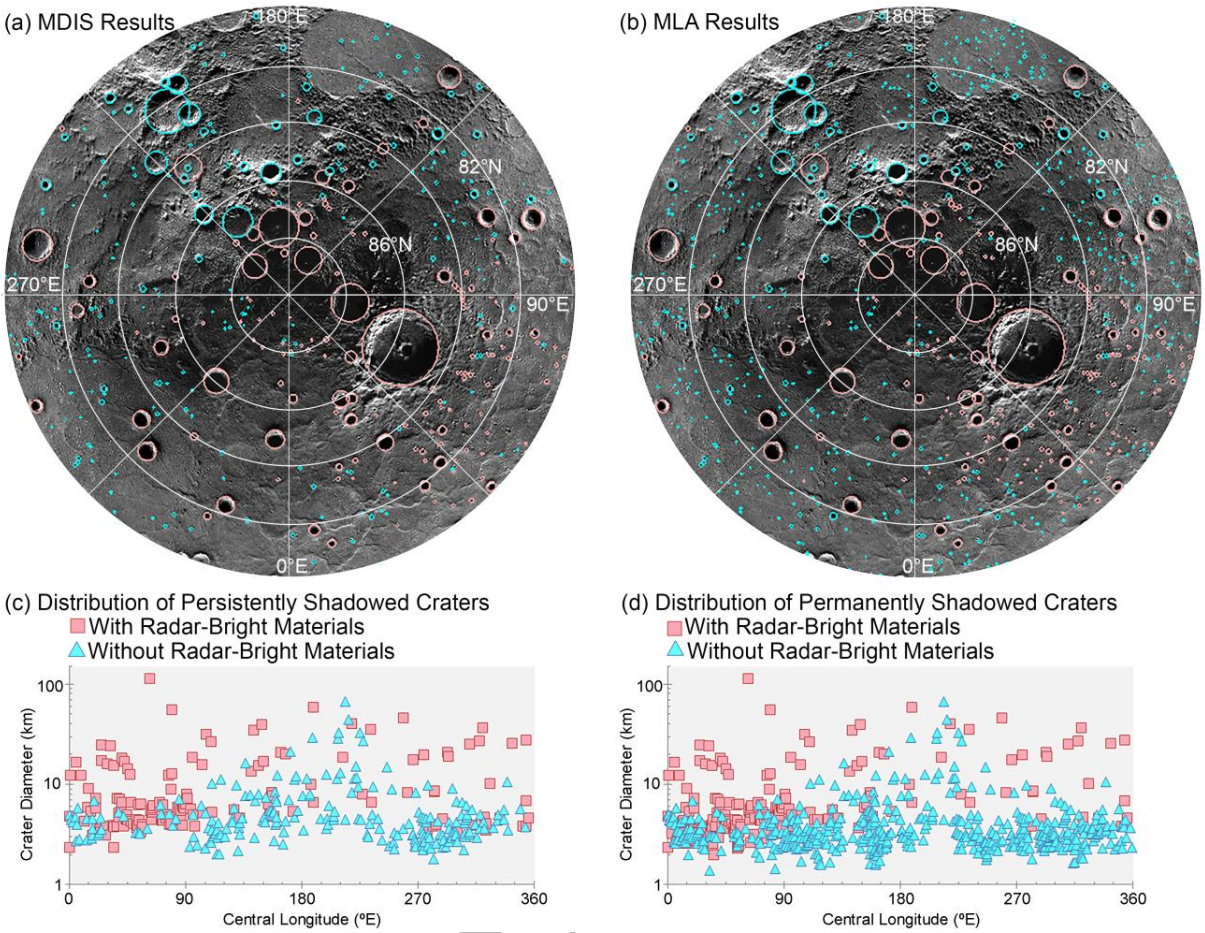

Fig. 8. Distribution of shadowed craters and radar-bright deposits shown on a mosaic of MESSENGER images from 80°N to 90°N in polar stereographic projection. (a) Craters identified as containing persistently shadowed areas in the MDIS-derived map. (b) Craters identified as containing permanently shadowed areas in the MLA-derived map. In (a) and (b), craters hosting radar-bright deposits are circled in coral, and those without radar-bright deposits are circled in cyan. (c) Distribution of persistently shadowed craters with longitude. (d) Distribution of permanently shadowed craters with longitude. In (c) and (d), craters hosting radar-bright deposits are represented with coral squares, and those without radar-bright materials are represented with cyan triangles.

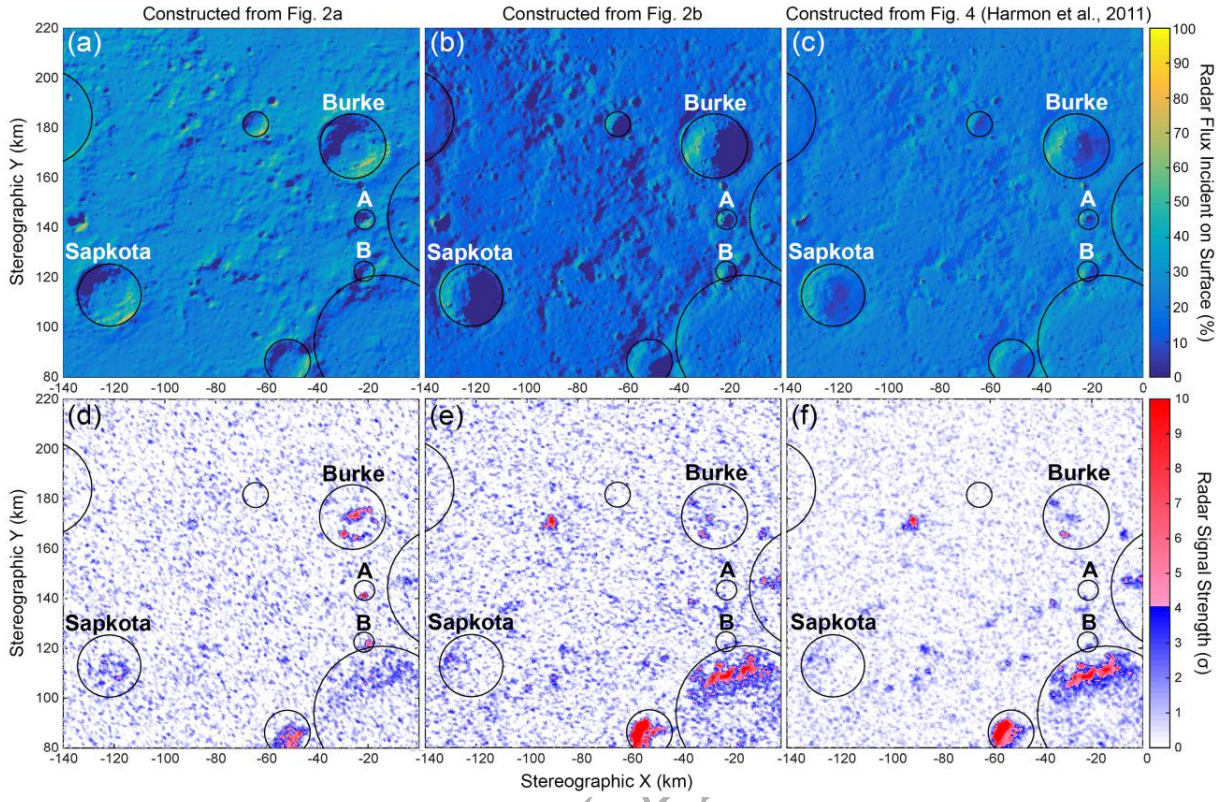

Fig. 9. A reconstruction of the viewing geometry with Earth-based radar for the region near Mercury's north pole that includes Burke and Sapkota craters. (a–c) The expected radar signal strength from the Earth-Mercury distance for the viewing geometries of Fig 2a, Fig. 2b, and Fig. 4 of Harmon et al. (2011), respectively. (d–f) Maps of radar return (see color bar at right) obtained from the specific observations from Fig. 2a, Fig. 2b, and Fig. 4 of Harmon et al. (2011). Areas with radar signal strength in excess of the adopted threshold of four standard deviations of the noise (4σ) are shaded in red. Unnamed craters A and B are also labeled.

Supplementary Figure Captions

Fig. S1. An average mosaic of Mercury's surface from 65°N to 90°N in polar stereographic projection at a pixel scale of 200 m.\

Fig. S2. A map of persistently shadowed regions derived from MDIS images from 65°N to 90°N in polar stereographic projection at a pixel scale of 200 m. Areas shadowed in all MDIS images of a given region are in white and have a pixel value of 1. Areas that are sunlit in any MDIS image are in black and have a pixel value of 0.

Fig. S3. A map of permanently shadowed regions derived from MLA topographic data from 65°N to 90°N in polar stereographic projection at a pixel scale of 200 m. Areas shadowed in the MLA model are in white and have a pixel value of 1. Areas that are modeled as sunlit are in black and have a pixel value of 0. The surrounding dark grey regions were not included in the model and have a null pixel value.

Fig. S4. Latitudinal distribution of (a) persistently shadowed regions derived from MDIS images, (b) permanently shadowed regions derived from MLA topographic data, and (c) radar-bright material from Harmon et al. (2011). Longitudinal distribution of (d) persistently shadowed regions derived from MDIS images, (e) permanently shadowed regions derived from MLA topographic data, and (f) radar-bright material from Harmon et al. (2011). Data for all graphs are from 65°N to 90°N and 0°E to 360°E in 1° bins.

Fig. S5. Radar image of polar deposits from Harmon et al. (2011) overlaid on a MESSENGER image mosaic from 80°N to 90°N in polar stereographic projection with a threshold of (a) 3 σ or (b) 4 σ, where σ is the standard deviation of the noise in the radar image.

Fig. S6. The expected strength of the radar return from Mercury received at the Arecibo Observatory, for the combined viewing geometries listed in Table 1 of Harmon et al. (2011). Regions modeled as radar-invisible to the Earth-based observations listed in Table 1 of Harmon et al. (2011) are shaded in red. Polar stereographic projection centered on Mercury's north pole.

Table 1

Comparison of regions of shadow and radar-bright deposits.

		65°N–90°N	80°N–90°N	85°N–90°N
Area of surface in shadow (%)	MDIS	1.06	3.73	13.4
	MLA	1.11	4.06	16.5
	South pole[1]			20
	Lunar north pole[2]		4.7	6.6
	Lunar south pole[2]		5.8	9.7
Surface that is radar bright (%)	3 σ threshold	1.39	3.61	12.9
	4 σ threshold	0.383	2.19	8.38
Radar-bright deposits* that are in shadow (%)	MDIS	77.5	78.9	75.4
	MLA	75.6	79.9	73.0
Shadowed terrain that is radar bright* (%)	MDIS	28.1	46.4	51.1
	MLA	26.3	43.2	44.4

[1]Chabot et al. (2012)

[2]Mazarico et al. (2011)

*From the Harmon et al. (2011) radar image with a threshold of 4 σ, where σ is the standard deviation of the noise in the image.

Table 2

Percent of shadowed craters that host radar-bright deposits from 80°N to 90°N.

		All	Hot pole	Cold pole	Hot pole	Cold pole	Thermally equivalent bins			
Longitudinal bins		0°E–360°E	315°E–45°E	45°E–135°E	135°E–225°E	225°E–315°E	0°E–90°E	90°E–180°E	180°E–270°E	270°E–360°E
All craters	MDIS	40.3	59.3	57.3	23.4	19.2	72.8	29.4	16.7	28.0
	MLA	29.4	42.6	43.4	13.9	10.3	60.0	18.6	9.17	14.7
< 10 km diameter	MDIS	34.8	52.1	53.9	14.3	13.5	68.4	21.6	9.09	20.5
	MLA	25.6	37.8	40.8	7.76	6.16	56.9	14.1	4.08	9.59
≥10 km diameter	MDIS	65.2	93.3	84.6	39.3	70.0	100	61.1	31.8	90.0
	MLA	65.2	93.3	84.6	39.3	70.0	100	61.1	31.8	90.0

Supplementary Tables

Table S1. Catalogue of all identifiable craters that are persistently shadowed, host radar-bright materials, or both in the MDIS-derived map. Each crater is sorted into one of three categories: "S" for craters that are identified as persistently shadowed, "S + RB" for craters that are in persistent shadow and host radar-bright deposits, and "RB" for craters that host radar-bright materials but are not identified as persistently shadowed.

Table S2. Catalogue of all identifiable craters that are permanently shadowed, host radar-bright materials, or both in the MLA-derived map. Each crater is sorted into one of three categories: "S" for craters that are identified as permanently shadowed, "S + RB" for craters that are in permanent shadow and host radar-bright deposits, and "RB" for craters that host radar-bright materials but are not modeled as permanently shadowed.